



CoO and g-C₃N₄ complement each other for highly efficient overall water splitting under visible light

Feng Guo^{a,b}, Weilong Shi^{a,c}, Cheng Zhu^a, Hao Li^a, Zhenhui Kang^{a,*}

^a Jiangsu Key Laboratory for Carbon-Based Functional Materials & Devices, Institute of Functional Nano & Soft Materials (FUNSOM), Soochow University, 199 Ren'ai Road, Suzhou, 215123, Jiangsu, PR China

^b Key Laboratory of Subsurface Hydrology and Ecological Effects in Arid Region, Ministry of Education, School of Environmental Science and Engineering, Chang'an University, Xi'an, 710064, PR China

^c School of Physics, Huazhong University of Science and Technology, Wuhan, 430074, PR China



ARTICLE INFO

Keywords:

CoO nanoparticles
g-C₃N₄
Photothermal deactivation
H₂O₂-resistence poisoning
Overall water splitting

ABSTRACT

Photocatalytic hydrogen production from overall water splitting is a clean and renewable technology that can convert solar energy into chemical energy, for which developing an efficient and stable photocatalyst has been the central scientific topic. Herein, CoO/g-C₃N₄ heterojunction photocatalysts were fabricated through a facile solvothermal method for overall water splitting. Simultaneous evolution of H₂ and O₂ from pure water with the stoichiometric ratio of about 2:1 achieved with all the CoO/g-C₃N₄ heterojunctions as catalysts under visible light irradiation. Among of them, 30 wt.% CoO/g-C₃N₄ with H₂ evolution rate of 2.51 μmol/h and O₂ evolution rate of 1.39 μmol/h also exhibited remarkably higher photocatalytic performance and stability (over 15 cycles) than single CoO or g-C₃N₄. This enhanced photocatalytic activity of CoO/g-C₃N₄ heterojunction can be ascribed to the synergistic effect of junction and interface formed between CoO and g-C₃N₄. In addition, the sufficient long lifetime stability of CoO/g-C₃N₄ comes from the complementary advantages effect between CoO and g-C₃N₄, as is proved, CoO can protect g-C₃N₄ from H₂O₂ poisoning, and simultaneously the photo-induced heat from CoO during the photocatalytic process responsible for the rapid deactivation can be timely conducted to g-C₃N₄.

1. Introduction

As a potential means of renewable energy production, photocatalytic water splitting under visible light has been considered as an advanced edge study in the current photocatalysis [1,2]. Since the pioneering work of Fujishima and Honda in 1972 [3], numerous semiconductor materials, such as metal oxides [4,5], nitrides [6], and sulfides [7], have been extensively studied for producing hydrogen from water. Nevertheless, most of developed single-component photocatalysts still suffer from kinds of limits, such as wide band gaps, instability and the rapid recombination of electron-hole pairs, etc [8,9]. In this case, enormous efforts have been made in tuning the semiconductor's interface and surface engineering. Sparked by the natural photosynthetic systems found in plant leaves, Z-scheme photocatalytic system consisting of two different photocatalysts is one of the most promising strategies to achieve water splitting [10]. In this concept, the water-splitting system can be separated into two parts: the photo-generated electrons in the higher conduction band for H₂ evolution and holes in the lower valence band (VB) for O₂ evolution, such as

MgTa₂O_{6-x}N_y/TaON [11], SrTiO₃:Rh/BiVO₄ [12], and RuO₂-TaON/Pt-TaON [13]. Another potential strategy to split water is loading cocatalysts (e.g. Pt [14], Ru [15], Rh [16] and transition metals [17]) on the surface of a semiconductor to promote its photocatalytic activity. In the view of this system, the metal cocatalyst acts like an electron trap to effectively separate the photogenerated charges, and suppress the back reaction of water formation from evolved H₂ and O₂. Apart from the above two systems, recent years have witnessed a flourish of interest in engineering heterojunctions in photocatalysts to split water under visible light irradiation. In the heterostructured system, heterojunction photocatalysts can not only extend visible-light response, but also promote efficiently spatial separation of the electron-hole pairs. For example, many heterojunction photocatalysts (e.g. CdS/TiO₂ [18], CuO/TiO₂ [19] and Bi₂S₃/TiO₂ [20], etc) have been reported for photocatalytic H₂ generation under visible light irradiation owing to the perfect band alignment and the highly efficient electron transfer. Although the construction of heterojunction photocatalysts provides a meritorious platform in the photocatalysis, recent engineering the heterojunction photocatalysts has mainly focused on how to effectively

* Corresponding author.

E-mail address: zhkang@suda.edu.cn (Z. Kang).

separate the electron-hole pairs based on the band structures of the semiconductors. Conversely, less emphasis is placed on the selection of semiconductors before engineering the heterojunction photocatalysts. In fact, it is very significant and should not be neglected besides the band energy alignments because every kind of semiconductors has its merits and demerits. In order to perfect the fabrication of heterojunction photocatalysts, it is significant to design a heterojunction photocatalyst not only possessing band energy alignments but also meeting complementary advantages of two photocatalysts for water splitting. As an example, we preliminary designed a CoO/g-C₃N₄ heterojunction photocatalyst to explain our idea.

Recent years, cobalt monoxide (CoO) photocatalyst has gained more attention since Bao et al. reported CoO exhibited overall water splitting with an extraordinary STH of around 5% in 2014 [21]. However, the fatal defect for CoO is severely deactivated, thus impeding its further practical application. Undoubtedly, solving the CoO deactivation has been of great importance in the photocatalysis [21,22]. So far, two main reasons leading to CoO deactivation have been reported, one of which corresponds to CoO nanoparticles aggregation, the other reason originates from the unintended thermo-induced oxidation of CoO during photocatalytic process [23]. Also, it should be particularly noted that we found that CoO photocatalyst possesses outstanding anti-H₂O₂ poisoning ability, which provides a new perspective in the design of H₂O₂-resistance composite photocatalysts to avoid many single-component photocatalysts poisoned by H₂O₂ [23]. Considering the reasons of CoO deactivation and its advantages, it stimulates us to make a new attempt to search for a semiconductor combined with CoO to form the heterojunction photocatalyst, which not only solves the deactivation of CoO but also takes advantage of CoO superiority. And the suitable semiconductor photocatalyst in this system should be equipped with favorable thermal conductivity for heat dispersion, larger specific surface area keeping nanoparticles from aggregation and suitable band gap against the recombination of electron-hole pairs.

Fortunately, graphitic carbon nitride (g-C₃N₄) with its unique thermal, electrical and optical properties and moderate band gap of around 2.7 eV has been extensively applied in the field of photocatalysis [24,25]. Particularly, g-C₃N₄ that consists exclusively of covalently-linked, sp²-hybridized carbon and nitrogen atoms not only possesses excellent thermal conductivity [26,27], but also could provide a large scaffold for anchoring various substrates to effectively prevent the aggregation of nanoparticles because of its large specific surface area and flexible 2D structure [28]. Nevertheless, apart from the main drawback of rapid recombination rate of electron-hole pairs, another fatal weakness of g-C₃N₄ can be attributed that it is easily subject to being seriously poisoned by the generating H₂O₂ during the photocatalysis, ultimately causing rapid inactivation [29,30]. Therefore, it is natural to conceive that coupling g-C₃N₄ with CoO to form a long-term stable and high-effective heterojunction photocatalyst by mutually compensating the respective deficiency.

In this work, we report that CoO/g-C₃N₄ heterojunction photocatalyst synthesized by one-step solvothermal method showed excellent photocatalytic activity for overall pure-water splitting. To clarify the effects of CoO content, both pristine CoO and g-C₃N₄ were also investigated. The results demonstrate that all the CoO/g-C₃N₄ heterojunctions exhibit much higher photocatalytic performance and outstanding stability compared to individual CoO and g-C₃N₄. And the highest photocatalytic activity was obtained when the CoO content reaches 30 wt.% in the composite, which exhibited H₂ evolution rate of 2.51 μmol/h and O₂ evolution rate of 1.39 μmol/h. Meanwhile, 30 wt.% CoO/g-C₃N₄ also displays the excellent durable photocatalytic stability (over 15 cycles). The enhanced photocatalytic activity of CoO/g-C₃N₄ photocatalyst can be predominantly resulted from the formed heterostructure between CoO and g-C₃N₄, which contributes to the efficient separation of photo-generated electrons and holes. The excellent durable photocatalytic stability of CoO/g-C₃N₄ heterojunction drives from the thermal conductivity of g-C₃N₄ and outstanding H₂O₂-resistance

property of CoO [23]. Additionally, g-C₃N₄ with large specific surface area and flexible 2D structure can effectively prevent CoO deactivation owing to the CoO nanoparticles aggregation.

2. Experimental section

2.1. Synthesis of CoO/g-C₃N₄ heterojunctions

The g-C₃N₄ powders were prepared through annealing urea in muffle according to our previous report [30]. Typically, 10 g of urea was put in an alumina crucible with a cover under ambient pressure in air, heated to 550 °C for 3 h with a ramping rate of 0.5 °C/min to complete the reaction. CoO/g-C₃N₄ heterojunctions with different mass ratios of CoO (10 wt.%, 20 wt.%, 30 wt.%, 40 wt.% and 50 wt.%) were synthesized using the following procedure: different mass ratios of Co (CH₃COO)₂·4H₂O (0.37, 0.83, 1.43, 2.22 and 3.33 g) and (1 g) g-C₃N₄ powders were added to a mixed solvent containing 16 mL n-octanol and 64 mL ethanol by stirring for 2 h. The resulted slurry was transferred to a 100 mL Teflon-lined stainless steel autoclave, and then heated at 220 °C for 4 h. When the autoclave was cooled down to room temperature, the formed powders were washed with ethanol for three times and finally dried at 70 °C in the oven. The CoO nanoparticles were fabricated under the same conditions in the absence of g-C₃N₄ powders.

2.2. Characterization

Powder X-ray diffraction (XRD) patterns of the samples were recorded using an X'Pert-ProMPD (olland) D/max- γ A X-ray diffractometer with Cu K α radiation ($\lambda = 0.154178$ nm). Transmission electron microscope (TEM), high-resolution TEM (HRTEM) and high-angle annular dark-field scanning transmission electron microscopy (HAADF-STEM) were performed with a FEI-Tecnai F20 microscope operating at 200 kV, respectively. Scanning electron microscopy (SEM) images were obtained with a FEI-quanta 200 microscope with an accelerating voltage of 20 kV. X-ray photoelectron spectroscopy (XPS) was performed on a KRATOS Axis ultra-DLD X-ray photoelectron spectrometer with a monochromatized Al K α X-ray source. Room temperature UV-vis absorption spectra were recorded on a Lambda 750 (Perkin Elmer) spectrophotometer in the wavelength range of 250–800 nm. Ultraviolet photoelectron spectroscopy (UPS) measurements were finished using an unfiltered He I (21.22 eV) gas discharge lamp and a total instrumental energy resolution of 100 meV. The Brunauer-Emmett-Teller (BET) specific surface areas and pore structures were characterized by a Micromeritics ASAP-2050 porosimeter. Photoluminescence (PL) study was recorded on a Fluorolog-TCSPC Luminescence Spectrometer. Electrochemical analysis was conducted on a CHI 660b workstation. The Pt wire, a calomel electrode, and the samples were served as the counter electrode, the reference electrode, and the working electrode in a three-electrode cell. Electrochemical impedance spectroscopy (EIS) was recorded by using an alternating voltage of 5 mV amplitude in the frequency range of 10⁵ Hz to 10⁻² Hz with the open circuit voltage in 0.5 M Na₂SO₄. For photocurrent versus time analysis and linear sweep voltammetry (LSV) curves, the Xenon lamp (100 mW cm⁻²) and Na₂SO₄ (0.1 M) were employed as light source and electrolyte, respectively.

2.3. Photocatalytic activity measurement

For photocatalytic reactions, 50 mg of photocatalyst, 20 mL of ultrapure water and a stir bar were put into a photoreactor vial with a total volume of 50 mL. Afterwards, the system was degassed to completely remove air. Under constant stirring, a white light-emitting diode (LED) was applied as the visible light source ($\lambda > 400$ nm). An online GC-7900 gas chromatograph (GC) set up with a thermal conductivity detector (TCD) and 5 Å molecular sieve columns was employed for the evolved gas detection. The temperatures of the oven, injection port and

detector in GC were held at 80, 100, and 120 °C, respectively. Ar was used as the carrier gas with a flow rate of 30 mL/min. For reproducibility and stability tests of the photocatalysts, the suspension after reaction was centrifuged and reused for repeated tests. The apparent quantum efficiency was estimated under a 300 W xenon lamp equipped with band pass filter (see the Supporting Information for details).

2.4. Heat-treatment of photocatalysts

In a typical synthesis run, 50 mg of the as-prepared photocatalysts were dispersed in 20 mL ultrapure water with further transfer into a 50 mL vial (the same one for photocatalytic reaction). Then, the suspension was treated by heating for 6 h under various temperatures (40, 50, 60, 70 and 80 °C) under air atmospheres.

2.5. Hydrogen peroxide (H_2O_2) generation test

Formation of H_2O_2 in the photocatalytic reaction system was detected by UV-vis spectroscopy using o-tolidine as the H_2O_2 indicator. 2 mL of the reaction supernatant was collected after centrifugation, and then 0.5 mL of 1% o-tolidine in 0.1 M HCl solution was added into it. After about 2 min, the dispersion was further acidified with 2 mL of 1 M HCl, if there is H_2O_2 existed in the solution, the color will change from transparent to yellow. Concentration of H_2O_2 was then obtained by measuring the absorbance of the yellow product at a characteristic peak wavelength of 436 nm.

3. Results and discussion

Fig. 1a shows the XRD patterns of g-C₃N₄, CoO and 30 wt.% CoO/g-C₃N₄. For g-C₃N₄ (blue trace), two pronounced peaks at 13.1° and 27.3° are found, which are in good agreement with graphitic phase carbon nitride [31]. The lower angle diffraction peak at 13.1° corresponds to tri-s-triazine units (100), and the other stronger one at 27.3° is derived from the interlayer stacking of aromatic segments (002). For CoO (black trace), all the diffraction peaks can perfectly match with the face-centered cubic CoO structure (JCPDS 71-1178) [32]. In the case of 30 wt.% CoO/g-C₃N₄ (red trace), all the diffraction peaks of both g-C₃N₄ and CoO can be observed in the XRD pattern. Furthermore, Fig. S1 displays the XRD patterns of all the as-prepared samples, indicating that with the increase of CoO concentration, the diffraction peaks intensity of CoO are more and more obvious, but two peaks belonging to g-C₃N₄ get weaker. In addition, composition and structure of g-C₃N₄, CoO and 30 wt.% CoO/g-C₃N₄ were further confirmed by FT-IR spectra (**Fig. 1b**). In the FT-IR spectrum of g-C₃N₄, the peak at near 808 cm⁻¹ is attributed to the characteristic breathing mode of tri-s-triazine units, and the peaks from 1200 to 1640 cm⁻¹ correspond to the typical stretching vibration modes of CN heterocycles. Another broad peak at around 3250 cm⁻¹ attributes to the stretching mode of N–H group at the defect sites of the aromatic ring [33]. With respect to CoO, the prominent peak

located at around 440 cm⁻¹ can be assigned to the stretching vibration of Co–O bond, and the other main band at around 3430 cm⁻¹ comes from the O–H stretching deformation [34]. After combining CoO with g-C₃N₄, all the main characteristic peaks of CoO and g-C₃N₄ appeared, testifying the coexistence of these two semiconductors in the composite, which is well consistent with the conclusion of XRD.

The SEM image of pure CoO is presented in **Fig. S2**, displaying that the as-prepared CoO consists of large-scale irregular nanoparticles with the diameters of 60–70 nm. The corresponding selective area electron diffraction (SAED) pattern (inset of **Fig. S2**) can further confirm the cubic crystal structure of CoO. **Fig. S3** shows the SEM image of g-C₃N₄, exhibiting a wrinkled-layer structure with several stacking layers. Interestingly, when CoO nanoparticles are evenly anchored on the g-C₃N₄ matrix, the morphology of CoO nanoparticles did not obviously change, but a big difference in their sizes. As shown in **Fig. 2a**, the typical size distributions of CoO embedded in the C₃N₄ matrix are in the range of 10–20 nm. The smaller particle sizes of CoO are mainly attributed to pre-adsorption of Co²⁺ onto the g-C₃N₄ surface, which restricts the growth of CoO particles [35]. In **Fig. 2b**, a clear lattice spacing of 0.25 nm can be assigned to the (111) crystal plane of CoO [36]. Furthermore, the results from HAADF-STEM image along with the elemental mapping images have demonstrated that the elements of C, N, Co and O are distributed in 30 wt.% CoO/g-C₃N₄ (**Fig. 2c** and d), which provides a solid evidence for the successful formation of a CoO/g-C₃N₄ heterostructure.

XPS was in-depth characterized to determine the specific bonding and chemical states of elements in 30 wt.% CoO/g-C₃N₄ photocatalyst. The full survey spectrum in **Fig. S4** indicates the 30 wt.% CoO/g-C₃N₄ is composed of C, N, Co, O and In elements. Particular attention should pay to In element, which is from the indium substrate. As shown in **Fig. 3a**, the high-resolution spectrum of Co 2p reveals two typical peaks located at 780.2 and 796.2 eV with another two relatively obvious satellite peaks (786.1 and 802.5 eV), which can be ascribed to the Co 2p_{3/2} and Co 2p_{1/2} spin-orbit peaks of CoO, respectively [21]. Meanwhile, the O 1s spectrum (**Fig. 3b**) can be subdivided into three peaks at 529.4, 531.2 and 533.1 eV, respectively. The binding energy at 529.4 eV is attributed to the Co–O bond in the CoO phase [37], while the peak at 531.2 eV corresponds to the Co–O–C bond [38], implying that a strong interaction exists between CoO and g-C₃N₄. The peak observed at 533.1 eV results from a small amount of physically adsorbed water molecules [39]. In the C 1s spectrum (**Fig. 3c**), three fine peaks located at 284.9, 285.8 and 288.3 eV are in good accordance with C–C coordination, sp³-coordinated carbon bonds and N–C=N coordination, respectively [40]. In **Fig. 3d**, the N 1s peak at 398.8 eV ascribes sp² hybridized aromatic N bonded to carbon atoms (C=N–C). While the other two peaks at 399.7 and 401.1 eV are attributed to the tertiary nitrogen N-(C)₃ groups and amino groups, respectively [41].

The optical properties of CoO, g-C₃N₄ and 30 wt.% CoO/g-C₃N₄ were examined by UV-vis diffuse reflectance spectroscopy and displayed in **Fig. 4a**. As can be seen, pure g-C₃N₄ (blue line) shows light

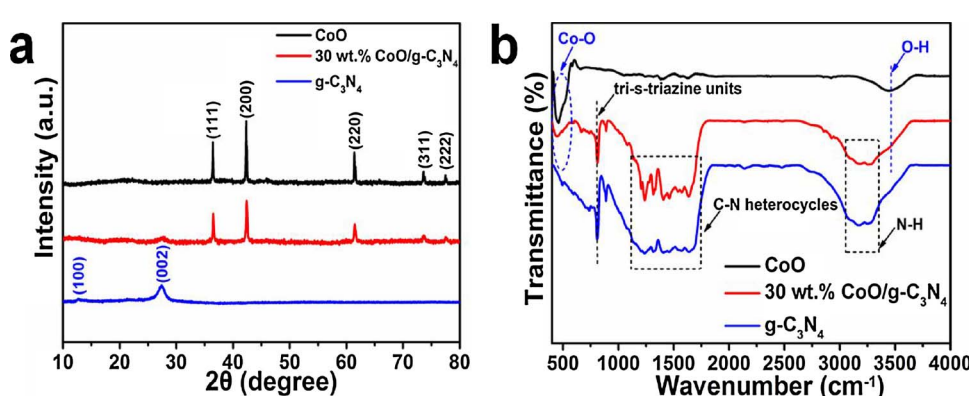


Fig. 1. (a) XRD patterns and (b) FT-IR spectra of g-C₃N₄, CoO and 30 wt.% CoO/g-C₃N₄.

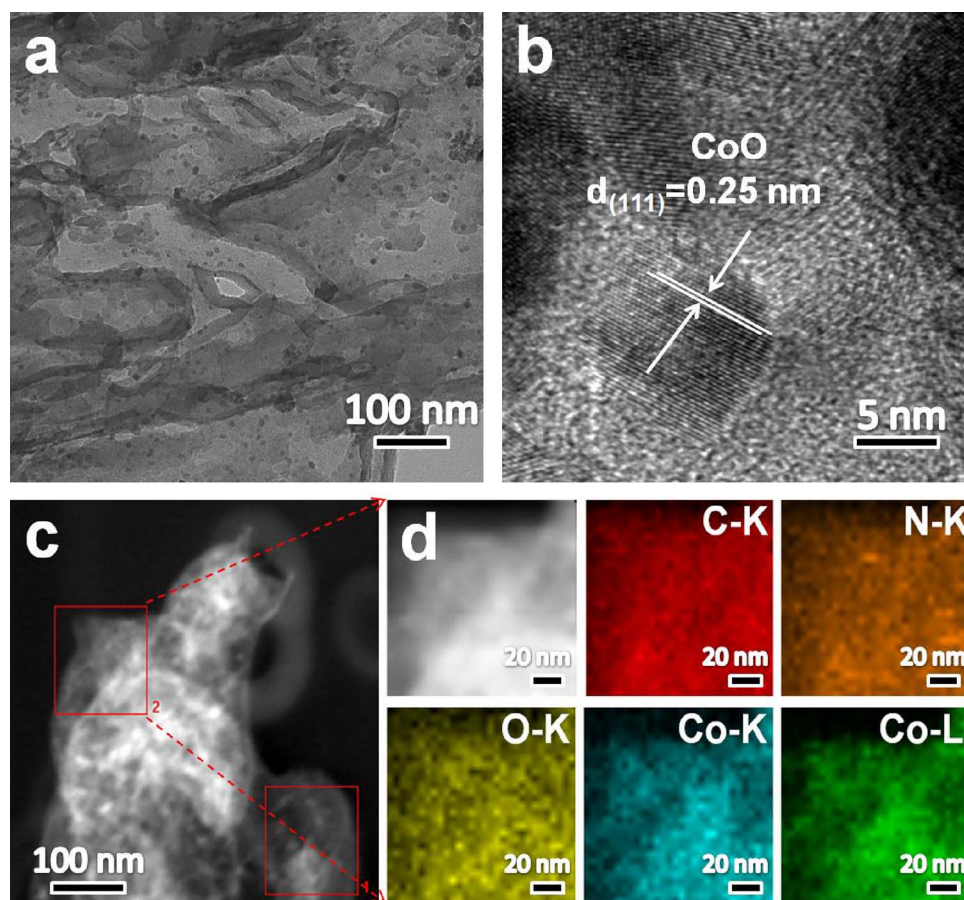


Fig. 2. (a) TEM image, (b) HRTEM image, (c) HAADF-STEM image, and (d) the corresponding elemental mapping images of 30 wt.% CoO/g-C₃N₄.

absorption below 450 nm and a weaker absorption tail in the visible-light region. The 30 wt.% CoO/g-C₃N₄ (red line) can absorb more visible light compared with that of g-C₃N₄, especially after 420 nm, which can be further verified by the color change of samples from pale

yellow for pure g-C₃N₄ (blue rectangle box in Fig. 4a) to light grayish for 30 wt.% CoO/g-C₃N₄ (red rectangle box in Fig. 4a), indicating that CoO to some extent enhances visible-light harvesting. The band gap energies estimated from the Tauc plots of CoO and g-C₃N₄ are

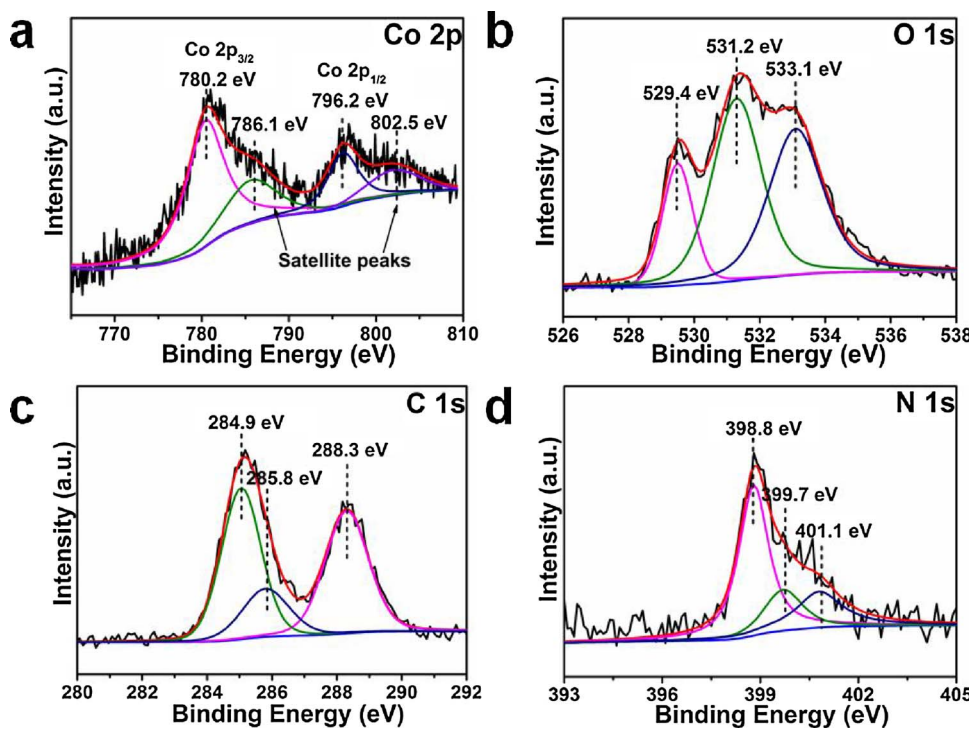


Fig. 3. High-resolution XPS spectra of 30 wt.% CoO/g-C₃N₄ of (a) Co 2p, (b) O 1s, (c) C 1s and (d) N 1s.

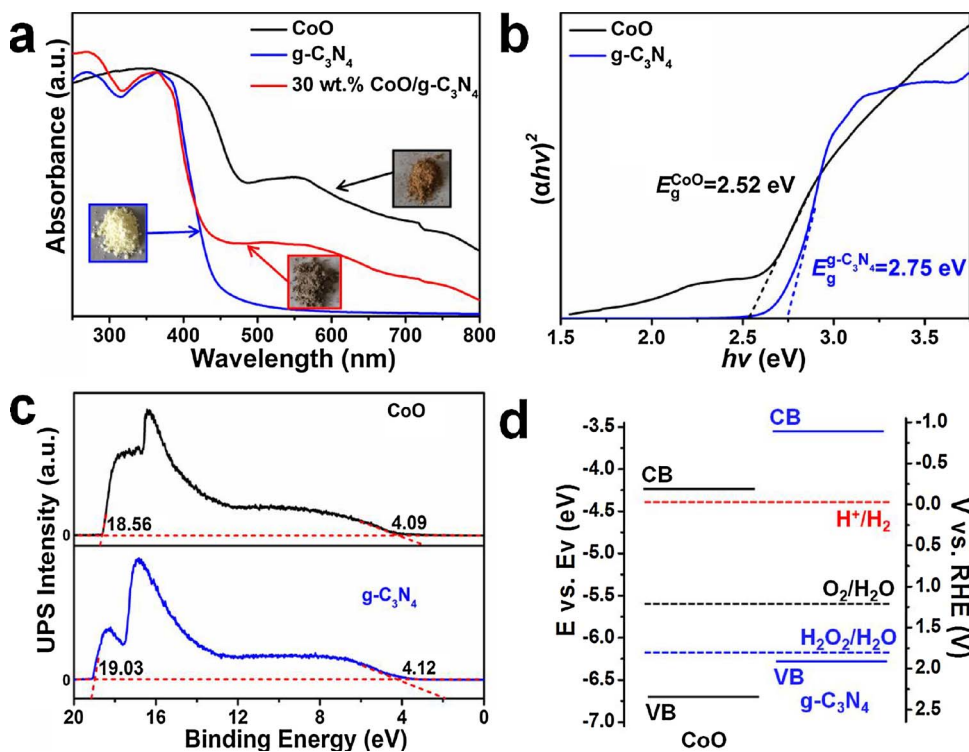


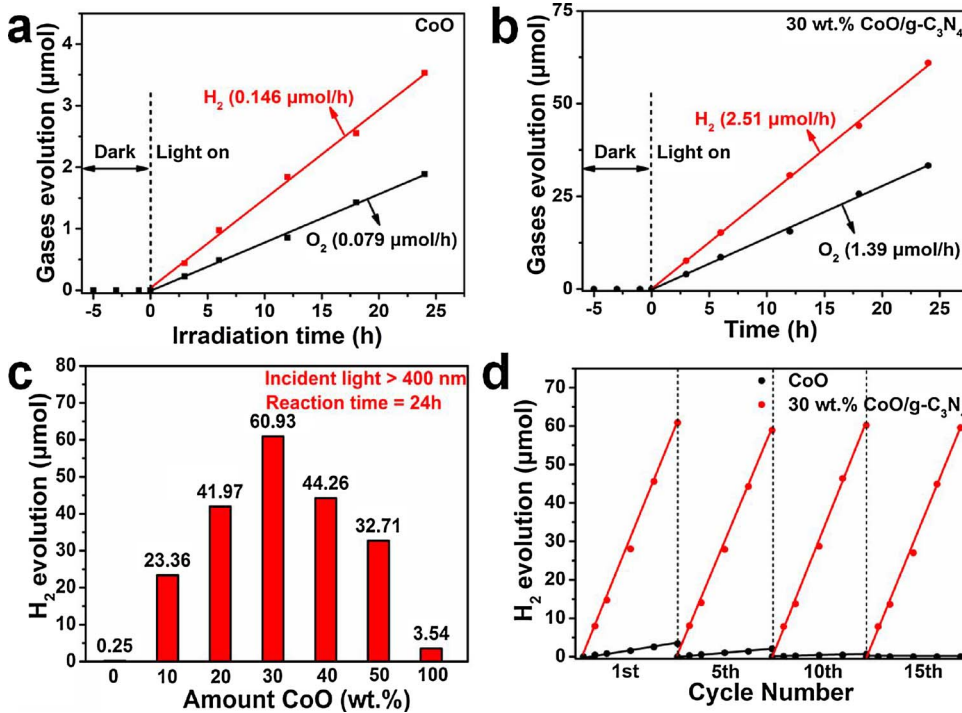
Fig. 4. (a) UV-vis spectra of g-C₃N₄, CoO and 30 wt. % CoO/g-C₃N₄. (b) Tauc plots of $(ahv)^2$ vs energy ($h\nu$) for the band gap energy of g-C₃N₄ and CoO. (c) UPS spectra and (d) the band structure diagrams of CoO and g-C₃N₄.

calculated to be 2.52 and 2.75 eV (Fig. 4b), respectively, which are consistent with the previous reported values of CoO and g-C₃N₄. Apart from a suitable band gap, the properly matched and positioned both conduction band and valence band levels of two semiconductors are also crucial and essential in designing a heterojunction photocatalyst. Fig. 4c shows the UPS spectra of CoO and g-C₃N₄ to determine their ionization potentials (equivalent to the E_{VB}), which are estimated to be 6.75 eV and 6.31 eV respectively by subtracting the width of the He I UPS spectra (21.22 eV). The E_{CB} of CoO and g-C₃N₄ are calculated to be 4.23 and 3.56 eV from $E_{VB}-E_g$, which equal to -0.21 and -0.88 V vs. RHE (reversible hydrogen electrode) after converting to electrochemical energy potentials in V, where 0 V vs. RHE equals -4.44 eV vs. vacuum level [30]. Fig. 4d shows the energy level diagrams of CoO and g-C₃N₄ compared to the potentials for the construction of heterojunction and water splitting. Obviously, the E_{VB} and E_{CB} positions of both CoO and g-C₃N₄ straddle H₂ reduction level, O₂ and H₂O₂ oxidation levels for water splitting. Meanwhile, the E_{CB} and E_{VB} of g-C₃N₄ are more negative than those of CoO, and this structure is propitious to the transfer of electrons and holes, indicating that the components of the heterojunction are suitably matched from the band structure. Based on the above analysis, CoO/g-C₃N₄ as a heterojunction photocatalyst can theoretically realize the overall water splitting into H₂, O₂ and H₂O₂.

In order to evaluate the performance of as-synthesized photocatalysts, the overall water splitting of the samples from pure water under visible light ($\lambda > 400$ nm) was carried out. The photocatalytic overall water splitting reactions using pristine CoO and 30 wt.% CoO/g-C₃N₄ are shown in Fig. 5a and b. Obviously, it is demonstrated that no H₂ and O₂ can be detected when the system is kept in the dark, but water can be decomposed into H₂ and O₂ with the approximately stoichiometric ratio of around 2:1 over pristine CoO and CoO/g-C₃N₄ under visible light irradiation. Particularly, H₂ production rate of 30 wt.% CoO/g-C₃N₄ (2.51 μ mol/h) is nearly seventeen times as high as that of pristine CoO (0.146 μ mol/h), giving a high AQE of 1.91% at 420 nm. Fig. S5 and Table S1 illustrate the decrease of AQE values with incident wavelengths (420, 450, 535 and 630 nm), which are in agreement with the absorption spectrum of 30 wt.% CoO/g-C₃N₄, indicating that the reaction is indeed a light-driven redox process. Furthermore, Fig. 5c

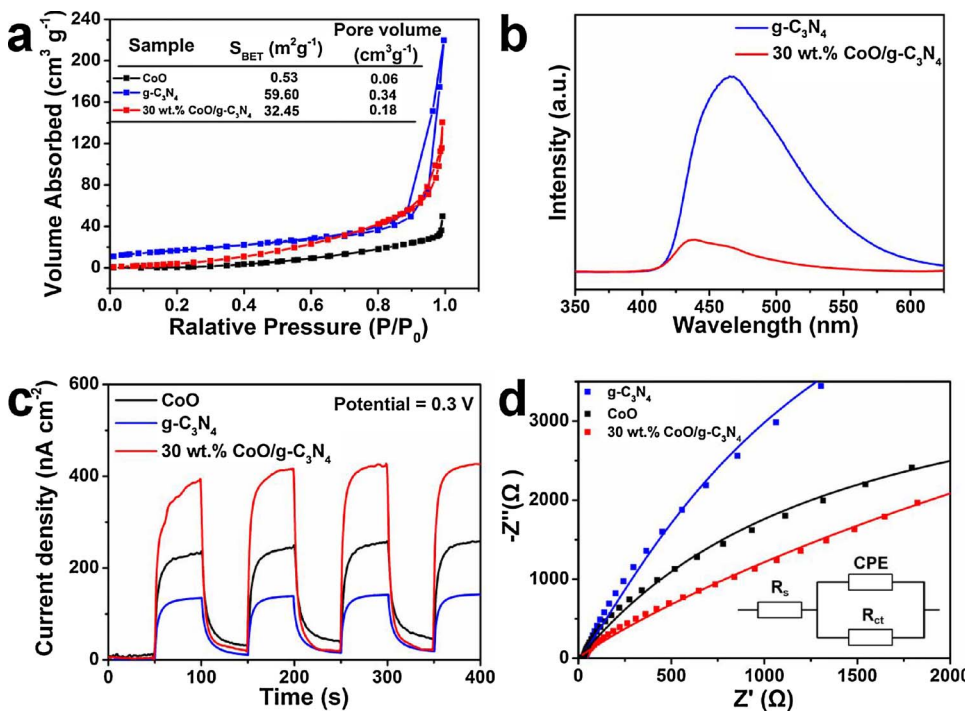
displays the photocatalytic H₂ evolutions from pure water over CoO/g-C₃N₄ composites with different CoO contents. It is evident that the photocatalytic H₂ production of g-C₃N₄ can be negligible (0.25 μ mol within 24 h), and this phenomenon may mainly attribute to the following reasons: (i) fast recombination of electron-hole pairs [42]; (ii) the produced H₂O₂ during the photocatalytic process leads to fast deactivation of g-C₃N₄ [29]. However, after combining CoO with g-C₃N₄, H₂ production evolution dramatically rises and the optimal content of CoO is obtained by 30 wt.%. Further increasing the content of CoO, H₂ production evolution of CoO/g-C₃N₄ reveals a somewhat decrease because of the shielding effect of the CoO, also suggesting that the introduction content of CoO does affect the photocatalytic activity in the CoO/g-C₃N₄ system. Again, the stabilities of CoO and 30 wt.% CoO/g-C₃N₄ were evaluated through recycling experiments under the same condition (Fig. 5d). It displays no apparent deactivation of the 30 wt.% CoO/g-C₃N₄ photocatalyst after fifteen recycles. Conversely, it is difficult to detect the H₂ production for pure CoO after five successive cycling experiments, demonstrating pure CoO is quite unstable. And this result concurs with our previous report [23]. To further investigate the stability of 30wt.% CoO/g-C₃N₄, Fig. S6a and b display that XRD patterns and high-resolution Co 2p XPS of 30 wt.% CoO/g-C₃N₄ before and after reactions, respectively. The intensities and positions of XRD and XPS peaks of 30 wt.% CoO/g-C₃N₄ before and after photocatalysis have no clear change, testifying CoO/g-C₃N₄ is a stable photocatalyst. Additionally, we also tested the hydrogen production over 30 wt.% CoO/g-C₃N₄ with different standing times (Fig. S7), showing that although 30 wt.% CoO/g-C₃N₄ sample is laid aside even for 60 days, it still keeps highly photocatalytic activity. Based on the above analysis, we can safely conclude that the as-prepared CoO/g-C₃N₄ heterojunctions indeed exhibit outstanding photocatalytic activity and stability.

For the sake of examining the mechanism for enhanced photocatalytic activity of CoO/g-C₃N₄ heterojunction photocatalyst, multiple techniques were carried out as follows. The BET adsorption isotherms of CoO, g-C₃N₄ and 30 wt.% CoO/g-C₃N₄ are displayed in Fig. 6a, where g-C₃N₄ ($59.60 \text{ m}^2 \text{ g}^{-1}$) shows a much higher specific surface area than 30 wt.% CoO/g-C₃N₄ ($32.45 \text{ m}^2 \text{ g}^{-1}$) and CoO ($0.53 \text{ m}^2 \text{ g}^{-1}$). This illustrates that the photocatalytic activities of as-prepared samples have



no positive correlation with the specific surface areas, suggesting the specific surface areas of the samples are not the main factor to enhance the photocatalytic performance in this work. Another factor that influences the photocatalytic activity attributes to the efficient separation of electron-hole pairs. It is widely accepted that heterostructure is more beneficial to enhanced photocatalytic activity due to a faster separation efficiency of photo-induced electrons and holes at the interfaces of heterojunctions. PL analysis is commonly applied to study the migration, transfer and recombination of electron-hole pairs generated by the photocatalyst [43]. The PL spectra of g-C₃N₄ and 30 wt.% CoO/g-C₃N₄ with excitation wavelength of 325 nm are shown in Fig. 6b. It can be

Fig. 5. H₂/O₂ evolutions from pure water with (a) CoO and (b) 30 wt.% CoO/g-C₃N₄ as photocatalysts. (c) H₂ evolutions of CoO/g-C₃N₄ with different contents of CoO. (d) The stability of photocatalytic water splitting over 30 wt.% CoO/g-C₃N₄. The photocatalytic reactions were performed with 50 mg of photocatalyst dispersed in 20 mL of ultrapure water under visible-light irradiation ($\lambda > 400$ nm).



seen that g-C₃N₄ exhibits a strong fluorescence emission peak at ~ 460 nm, while the PL intensity of g-C₃N₄ (still at ~ 460 nm) distinctly decreased after introducing CoO. The lower PL intensity necessarily manifests a slower recombination rate of electron-hole pairs, which indicates a fast interfacial charge transfer between g-C₃N₄ and CoO in the CoO/g-C₃N₄ heterojunctions. Besides, the interfacial charge efficient separation is further verified by the photoelectrochemical technique. Fig. S8 shows the linear sweep voltammetry (LSV) curves of prepared samples which were carried out under xenon lamp irradiation in 0.1 M Na₂SO₄ aqueous solution. Clearly, as-prepared 30 wt.% CoO/g-C₃N₄ exhibited significantly improved photo-response under light

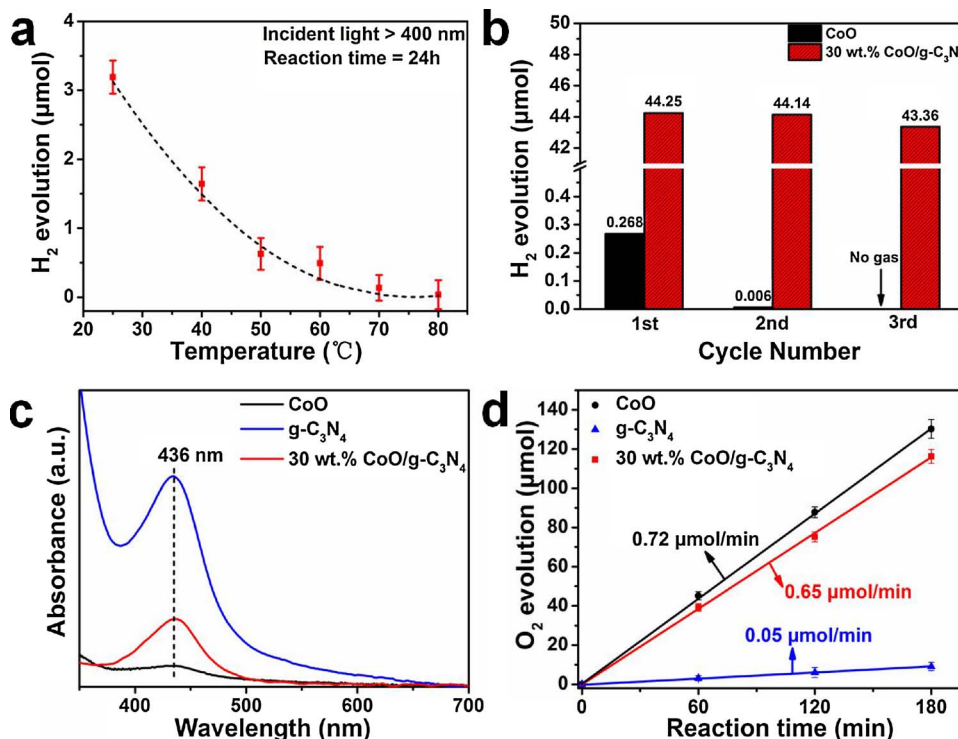
Fig. 6. (a) Nitrogen sorption isotherm and measured parameters (inset) of CoO, g-C₃N₄ and 30 wt.% CoO/g-C₃N₄. (b) The PL spectra of g-C₃N₄ and 30 wt.% CoO/g-C₃N₄ at excitation wavelength of 325 nm. (c) Photocurrent response versus time of as-prepared CoO, g-C₃N₄ and 30 wt.% CoO/g-C₃N₄ in 0.1 M Na₂SO₄ under xenon lamp irradiation (0.3 V vs. SCE, 100 mW cm⁻²). (d) EIS curves of as-prepared CoO, g-C₃N₄ and 30 wt.% CoO/g-C₃N₄.

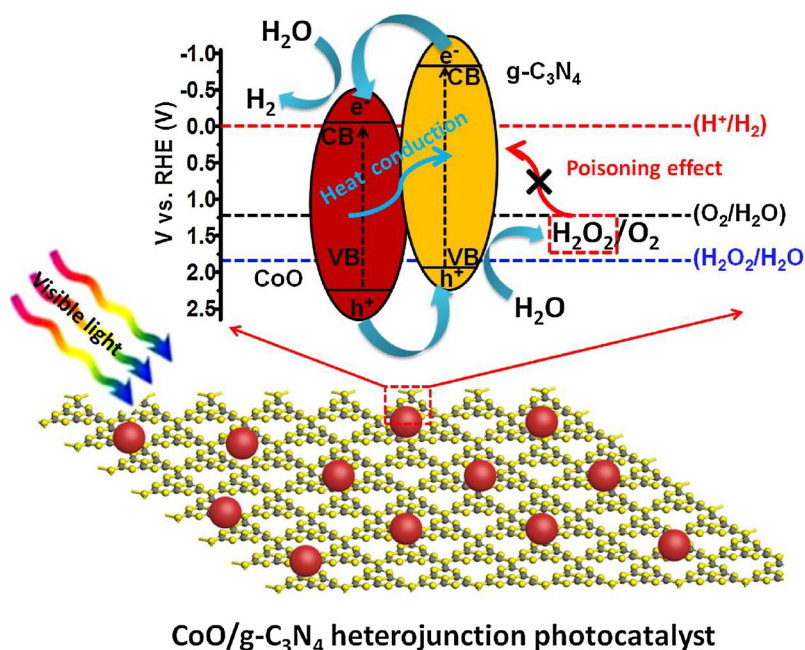
illumination, and the saturation photocurrent reaches 420 nA cm^{-2} at 0.3 V (vs. SCE), nearly 1.85 and 3 times higher than that of pristine CoO (227 nA cm^{-2}) and g-C₃N₄ (140 nA cm^{-2}) at the same condition, respectively. Furthermore, transient photocurrent responses were conducted in the same electrolytes with interval 50 s light on/off cycle at 0.3 V (vs. SCE) shown in Fig. 6c. The as-prepared 30 wt.% CoO/g-C₃N₄ exhibited excellent photo-stability after 400 s test and achieved higher photocurrent than their sole components, revealing that the existence of heterojunction structure is beneficial to the electron transfer and separation process. EIS measurements of CoO, g-C₃N₄, and 30 wt.% CoO/g-C₃N₄ were also conducted as shown in Fig. 6d, offering additional evidence for the enhanced charge separation in the CoO/g-C₃N₄ heterojunction. It can be clearly observed that EIS Nyquist plot of 30 wt.% CoO/g-C₃N₄ heterojunction has the smallest arc radius in comparison with that of pure g-C₃N₄ and CoO. The Nyquist plot was also fitted to the equivalent Randle circuit (inset in Fig. 6d) for further analyzing the impedance spectra, where R_s is the electrolyte solution resistance, CPE is the constant phase element for the electrode and electrolyte interface, and R_{ct} is the interfacial charge transfer resistance across the electrode/electrolyte [44]. It signifies that 30 wt.% CoO/g-C₃N₄ exhibited the fastest interfacial charge transfer and the most efficient separation of photo-generated charge carriers.

Moreover, we explored the reasons for the high stability of CoO/g-C₃N₄. Sparked by our recent report, experimental results demonstrated that the deactivation of sub-micrometer CoO octahedron photocatalysts resulted from the unintended thermo-induced oxidation during photocatalysis [23]. Similarly, we also further investigated the deactivation reason of CoO nanoparticles in this work. Fig. 7a shows that with increasing the treated temperature, the photocatalytic H₂ production of CoO nanoparticles from pure water rapidly declines. When the treated temperature reached to 80°C , 24 h photocatalytic H₂ evolution of pure CoO is hardly to be detected. As expected, 30 wt.% CoO/g-C₃N₄ exhibits excellent heat resistance. It shows that 70°C treated 30 wt.% CoO/g-C₃N₄ still continues to generate hydrogen without obvious decrease after three cycles (Fig. 7b). The result partly benefited from the favorable heat conductor of g-C₃N₄, which extremely degrades the photo-induced heating of CoO during the photocatalytic reaction.

Meanwhile, from the TEM of 30 wt.% CoO/g-C₃N₄ (Fig. 2a), all the CoO nanoparticles are averagely on the surface of g-C₃N₄, thus avoiding the aggregation of CoO, which also protects CoO from the deactivation. Additionally, it should particularly consider another factor is that the existence of H₂O₂ in water splitting process, which may poison g-C₃N₄ in this complex photocatalytic system. H₂O₂ in the reaction solution using CoO, g-C₃N₄ and 30 wt.% CoO/g-C₃N₄ as photocatalysts were reflected by UV-vis absorption spectra, where H₂O₂ were detected in all the photocatalytic systems (Fig. 7c). Unexpectedly, photocatalytic H₂ evolution activity of 30 wt.% CoO/g-C₃N₄ lasts as long as fifteen cycles (Fig. 5d), indicating that CoO may play certain roles in the CoO/g-C₃N₄. Thus, we tested the photocatalytic H₂ production of CoO nanoparticles with purposefully adding H₂O₂ from 0.01 to 0.24 mol/L , which expectedly indicates no apparent decrease (Fig. S9). The result proves CoO nanoparticles possess excellent H₂O₂-resistance poisoning property. Thus, we inferred that when CoO coupled with g-C₃N₄, CoO protected g-C₃N₄ from being poisoned through H₂O₂ decomposition. In the next experiment, we further characterized the evaluation of O₂ evolution from H₂O₂ decomposition versus time in the 10 mM H₂O₂ under dark using CoO, 30 wt.% CoO/g-C₃N₄ and g-C₃N₄ as catalysts. It is found that the O₂ evolution rate of 30 wt.% CoO/g-C₃N₄ is $0.65 \mu\text{mol}/\text{min}$, much higher than that of g-C₃N₄ ($0.05 \mu\text{mol}/\text{min}$), and CoO exhibits the highest O₂ evolution rate ($0.72 \mu\text{mol}/\text{min}$) in Fig. 7d. As a consequence, CoO and 30 wt.% CoO/g-C₃N₄ possess the outstanding ability for the H₂O₂ decomposition under dark. Based on the above experimental results, we can further conclude that the impressive stability of CoO/g-C₃N₄ can be attributed to the excellent heat conducting property and large specific surface area of g-C₃N₄, and H₂O₂-resistance property of CoO nanoparticles.

Considering the above analysis and experimental results, a possible photocatalytic mechanism for overall water splitting over CoO/g-C₃N₄ heterojunction photocatalyst was proposed (Fig. 8). And this enhanced and stable photocatalytic activity of CoO/g-C₃N₄ can be attributed to the complementary advantages between g-C₃N₄ and CoO in the following reasons: under visible light irradiation, both CoO and g-C₃N₄ can be excited to generate electrons and holes. Moreover, the excited electrons transfer from the CB of g-C₃N₄ to that of CoO, while the holes





in the VB of CoO transfer to the VB of g-C₃N₄ due to the well matched band structures of CoO and g-C₃N₄. The accumulated electrons on the surface of CoO tend to combine with H₂O to produce H₂ since the CB (−0.21 V vs. RHE) of CoO is more negative than the reduction potential of H⁺ to H₂ (0 V vs. RHE), and holes on the surface of g-C₃N₄ will react with H₂O to generate O₂ and H₂O₂, which attributes to the more positive VB of g-C₃N₄ (1.87 vs. RHE) than O₂/H₂O (1.23 V vs. RHE) and H₂O₂/H₂O (1.78 V vs. RHE). During the photocatalytic reaction, the unintended produced heating of CoO timely transmits to g-C₃N₄ owing to the excellent thermal conductivity property of g-C₃N₄, simultaneously, outstanding resistance to H₂O₂ poisoning of CoO immediately decomposes H₂O₂ to protect g-C₃N₄ from being poisoned.

4. Conclusion

The CoO/g-C₃N₄ heterojunction photocatalysts were fabricated through a facile solvothermal method. In comparison to the single CoO and g-C₃N₄, the CoO/g-C₃N₄ heterojunction photocatalysts exhibited enhanced photocatalytic activity and long-term stability for overall water splitting under visible light. The optimum photocatalytic activity with approximate stoichiometric ratio of H₂ evolution rate of 2.51 μmol/h and O₂ evolution rate of about 1.39 μmol/h was obtained by the CoO/g-C₃N₄ heterojunctions with a CoO mass content of 30 wt %. The enhanced photocatalytic activity should be attributed to the effective separation of photogenerated electron-hole pairs in CoO/g-C₃N₄ heterostructure. And the durable stability is derived from the complementary advantages between CoO and g-C₃N₄, in which CoO keeps g-C₃N₄ from being poisoned by H₂O₂, on the contrary, the produced unintended heat from CoO during the photocatalytic reaction is extremely ameliorated after combining with g-C₃N₄ as a heat conductor. Additionally, g-C₃N₄ with large specific surface area and flexible 2D structure could effectively prevent CoO aggregation. We anticipate that our idea will provide a new insight of designing heterojunction photocatalysts for photocatalytic hydrogen production to meet the energy demands in the near future.

Acknowledgements

This work is supported by the Collaborative Innovation Center of Suzhou Nano Science and Technology, the National Natural Science Foundation of China (51725204, 21771132, 51422207, 51572179,

Fig. 8. The possible photocatalytic mechanism for overall water splitting over CoO/g-C₃N₄ heterojunction photocatalyst.

21471106, 21501126), the Natural Science Foundation of Jiangsu Province (BK20161216) and a project funded by the Priority Academic Program Development of Jiangsu Higher Education Institutions (PAPD).

Appendix A. Supplementary data

Supplementary data associated with this article can be found, in the online version, at <https://doi.org/10.1016/j.apcatb.2017.12.064>.

References

- [1] Y.P. Yuan, L.W. Ruan, J. Barber, S.C.J. Loo, C. Xue, Energy Environ. Sci. 7 (2014) 3934–3951.
- [2] A. Kudo, Y. Miseki, Chem. Soc. Rev. 38 (2009) 253–278.
- [3] A. Fujishima, K. Honda, Nature 238 (1972) 37.
- [4] D. Mateo, I. Esteve-Adell, J. Albero, A. Primo, H. García, Appl. Catal. B: Environ. 201 (2017) 582–590.
- [5] Y. Ham, T. Hisatomi, Y. Goto, Y. Moriya, Y. Sakata, A. Yamakata, J. Kubota, K. Domen, J. Mater. Chem. A 4 (2016) 3027–3033.
- [6] J. Xu, C. Pan, T. Takata, K. Domen, Chem. Commun. 51 (2015) 7191–7194.
- [7] F. Vaquero, R.M. Navarro, J.L.G. Fierro, Appl. Catal. B: Environ. 203 (2017) 753–767.
- [8] J. Zhang, Q. Xu, Z. Feng, M. Li, C. Li, Angew Chem. Int. Ed. 47 (2008) 1766–1769.
- [9] E.S. Kim, N. Nishimura, G. Mageesh, J.Y. Kim, J.W. Jang, H. Jun, J. Kubota, K. Domen, J.S. Lee, J. Am. Chem. Soc. 135 (2013) 5375–5383.
- [10] A.J. Bard, J. Photochem. 10 (1979) 59–75.
- [11] S. Chen, Y. Qi, T. Hisatomi, Q. Ding, T. Asai, Z. Li, S.S. Ma, F. Zhang, K. Domen, C. Li, Angew Chem. Int. Ed. 54 (2015) 8498–8501.
- [12] A. Iwase, Y.H. Ng, Y. Ishiguro, A. Kudo, R. Amal, J. Am. Chem. Soc. 133 (2011) 11054–11057.
- [13] K. Maeda, R. Abe, K. Domen, J. Phys. Chem. C 115 (2011) 3057–3064.
- [14] S.R. Lingampalli, U.K. Gautam, C.N.R. Rao, Energy Environ. Sci. 6 (2013) 3589.
- [15] M. Hara, J. Nunoshige, T. Takata, J.N. Kondo, K. Domen, Chem. Commun. (2003) 3000.
- [16] Y. Sasaki, A. Iwase, H. Kato, A. Kudo, J. Catal. 259 (2008) 133–137.
- [17] W.J. Youngblood, S.H.A. Lee, Y. Kobayashi, E.A. Hernandez-Pagan, P.G. Hoertz, T.A. Moore, A.L. Moore, D. Gust, T.E. Mallouk, J. Am. Chem. Soc. 131 (2009) 926–933.
- [18] J. Jang, H. Kim, U. Joshi, J. Jang, J. Lee, Int. J. Hydrogen Energy 33 (2008) 5975–5980.
- [19] W.-T. Chen, V. Jovic, D. Sun-Waterhouse, H. Idriss, G.I.N. Waterhouse, Int. J. Hydrogen Energy 38 (2013) 15036–15048.
- [20] C. García-Mendoza, S. Oros-Ruiz, A. Hernández-Gordillo, R. López, G. Jácome-Acatitla, H.A. Calderón, R. Gómez, J. Chem. Technol. Biotechnol. 91 (2016) 2198–2204.
- [21] L. Liao, Q. Zhang, Z. Su, Z. Zhao, Y. Wang, Y. Li, X. Lu, D. Wei, G. Feng, Q. Yu, X. Cai, J. Zhao, Z. Ren, H. Fang, F. Robles-Hernandez, S. Baldelli, J. Bao, Nat. Nanotechnol. 9 (2014) 69–73.
- [22] X. Zhan, Z. Wang, F. Wang, Z. Cheng, K. Xu, Q. Wang, M. Safdar, J. He, Appl. Phys. Lett. 105 (2014) 153903.

- [23] W. Shi, F. Guo, H. Wang, S. Guo, H. Li, Y. Zhou, C. Zhu, Y. Liu, H. Huang, B. Mao, Y. Liu, Z. Kang, ACS Appl. Mater. Inter. 9 (2017) 20585–20593.
- [24] P. Niu, L.L. Zhang, G. Liu, H.M. Cheng, Adv. Funct. Mater. 22 (2012) 4763–4770.
- [25] X. Wang, K. Maeda, A. Thomas, K. Takanabe, G. Xin, J.M. Carlsson, K. Domen, M. Antonietti, Nat. Mater. 8 (2009) 76–80.
- [26] D.T. Morelli, J.P. Heremans, Appl. Phys. Lett. 81 (2002) 5126–5128.
- [27] B. Mortazavi, G. Cuniberti, T. Rabczuk, Comp. Mater. Sci. 99 (2015) 285–289.
- [28] S. Kumar, T. Surendar, B. Kumar, A. Baruah, V. Shanker, J. Phys. Chem. C 117 (2013) 26135–26143.
- [29] J. Liu, N.Y. Liu, H. Li, L.P. Wang, X.Q. Wu, H. Huang, Y. Liu, F. Bao, Y. Lifshitz, S.T. Lee, Z.H. Kang, Nanoscale 8 (2016) 11956–11961.
- [30] J. Liu, Y. Liu, N. Liu, Y. Han, X. Zhang, H. Huang, Y. Lifshitz, S.T. Lee, J. Zhong, Z. Kang, Science 347 (2015) 970–974.
- [31] F. Guo, W. Shi, W. Guan, H. Huang, Y. Liu, Sep. Purif. Technol. 173 (2017) 295–303.
- [32] Q. Qi, Y. Chen, L. Wang, D. Zeng, D.L. Peng, Nanotechnol 27 (2016) 455602.
- [33] W. Shi, F. Guo, J. Chen, G. Che, X. Lin, J. Alloy Compd. 612 (2014) 143–148.
- [34] H. Shi, X. He, J. Phys. Chem. Solids 73 (2012) 646–650.
- [35] P. Suyana, P. Ganguly, B.N. Nair, A.P. Mohamed, K.G.K. Warrier, U.S. Hareesh, Environ. Sci.: Nano 4 (2017) 212–221.
- [36] X. Guan, J. Nai, Y. Zhang, P. Wang, J. Yang, L. Zheng, J. Zhang, L. Guo, Chem. Mater. 26 (2014) 5958–5964.
- [37] Y. Sun, Y. Zhou, C. Zhu, L. Hu, M. Han, A. Wang, H. Huang, Y. Liu, Z. Kang, Nanoscale 9 (2017) 5467–5474.
- [38] Q.M. Yu, J.X. Xu, C.Y. Wan, C.X. Wu, L.H. Guan, J. Mater. Chem. A 3 (2015) 16419–16423.
- [39] S. Xiong, J.S. Chen, X.W. Lou, H.C. Zeng, Adv. Funct. Mater. 22 (2012) 861–871.
- [40] X. Lu, K. Xu, P. Chen, K. Jia, S. Liu, C. Wu, J. Mater. Chem. A 2 (2014) 18924–18928.
- [41] S. Thaweesak, M. Lyu, P. Peerakiatkajohn, T. Butburee, B. Luo, H. Chen, L. Wang, Appl. Catal. B: Environ. 202 (2017) 184–190.
- [42] Q. Han, B. Wang, J. Gao, L.T. Qu, Angew Chem. Int. Ed. 55 (2016) 10849–10853.
- [43] Y.M. He, L.H. Zhang, B.T. Teng, M.H. Fan, Environ. Sci. Technol. 49 (2015) 649–656.
- [44] J. Xu, L.W. Zhang, R. Shi, Y.F. Zhu, J. Mater. Chem. A 1 (2013) 14766–14772.